JOINT EUROPEAN TORUS

JET–P(90)26

G.T.A. Huysrnans, T.C. Hender, O.J. Kwon, J.P. Goedbloed,
E. Lazzaro, P. Smeulders and JET Team

MHD Stability Analysis of High-Beta JET Discharges

MHD Stability Analysis of High-Beta JET Discharges

G.T.A. Huysrnans[1], T.C. Hender[2], O.J. Kwon[2] J.P. Goedbloed[1],
E. Lazzaro[3], P. Smeulders and JET Team*

JET-Joint Undertaking, Culham Science Centre, OX14 3DB, Abingdon, UK

[1]EURATOM/FOM Association, FOM Instituut voor Plasmafysica, Nieuwegein, The Netherlands
[2]UKAEA/EURATOM Fusion Association, Culham Laboratory, Abingdon, UK
[3]Present address: Bassini 15, Milano, Italy
** See Appendix 1*

Preprint of Paper to be submitted for publication in
Plasma Physics and Controlled Nuclear Fusion

MHD STABILITY ANALYSIS OF HIGH–β JET DISCHARGES

G.T.A.Huysmans[+], T.C.Hender[*], O.J.Kwon[*], J.P.Goedbloed[+], E.Lazzaro[x] and P.Smeulders.
JET Joint Undertaking, Abingdon, OX143EA, UK.

[*]UKAEA/EURATOM Fusion Association, Culham Laboratory, Abingdon, UK.
[+] EURATOM/FOM Association, FOM Instituut voor Plasmafysica, Nieuwegein, The Netherlands
[x] Present address Bassini 15, Milano, Italy.

Abstract

The theoretical stability of high–β JET discharges is discussed. For high–n ballooning modes near the β–limit, it is found that approximately the central 50% of the plasma is marginally stable. For low–n modes ($n = 1$ and 2) the theoretical predictions are found to correlate well with the experimentally observed soft X-ray behaviour, and provide a basis for predicting the central q–profile.

I Introduction

Recent high–β discharges in JET [Smeulders et al 1990] have reached values of β up to the Troyon limit [Troyon et al 1984] ($\beta_{Troyon}(\%) = 2.8I(MA)/B(T)a(m)$); here β is the ratio of volume average kinetic pressure to equilibrium toroidal magnetic field pressure. These high–β values were reached in double null X-point configurations during the H-mode. To reduce the total heating power needed to obtain these high β's, a low toroidal field ($B_T \sim 1.0 - 1.5$T) was used. At, or near, the β–limit two general categories of MHD behaviour were found. Most commonly the β would saturate and associated with this, periodic bursts of oscillating MHD phenomena in the plasma center (fishbones and sawteeth) and oscillating MDH phenomena at the plasma edge (higher n mode numbers) were observed. An example of this, for the shot with the highest β to date, is shown in Fig 1 where the sawteeth and (smaller) fishbone events are evident on the central soft X–ray (SXR) chord; the effects of these events on β is also evident. Less commonly ($\sim 30 - 40\%$ of shots) a large low-n instability (usually $n = 2$) would be destabilised and an apparently correlated collapse of β occured (here n is the toroidal mode number). These experimental features are described in more detail by Smeulders et al (1990). In this paper we discuss the theoretical ideal and resistive MHD stability properties of these discharges, and comparisons with observed mode structures.

The remainder of this paper is organised as follows. In the next section brief details of equilibrium reconstruction techniques and stability codes are given. Then in Sections III

and IV respectively, high–n and low–n stability studies are described. Finally in Section V a summary of the results is given.

II Equilibrium and Stability Codes

The equilibria needed for the stability studies are in general calculated with the IDENT–C code [Blum et al 1986, Lazzaro and Mantica 1988] which fits the magnetic measurements and the experimental pressure profile. The pressure profile shape is generally taken from the LIDAR electron pressure measurements and normalised to match the diamagnetic β. This is a reasonable approximation as the electron and ion pressure profiles shapes are generally quite similar in these high–β discharges. It does however mean that the contribution to β from fast particles is included.

The high–n ballooning mode stability of these equilibria has been studied with the HBT (Goedbloed 1981 and 1984, Huysmans 1990) and ERATO (Gruber 1981) codes, the results being in good agreement. In both these codes the normal ballooning mode transformation (Connor, Hastie and Taylor 1978) is employed, which reduces the evaluation of high–n ballooning stability to solving an eigenvalue problem on each equilibrium flux surface. The low–n free boundary ideal stability has also been studied with the HBT and ERATO codes. To examine low–n internal instabilities the fixed boundary resistive MHD code, FAR (Charlton et al 1990) has been used.

III Ballooning Stability

In this section we will discuss the ballooning mode stability of two types of high-β discharges. For the first type of discharge with peaked pressure profiles, we will analyse a case with a triangular pressure profile and one with large central pressure gradients caused by the injection of a pellet. The second type of discharge has a broader pressure profile with the larger gradients near the plasma boundary.

The pressure profile typically develops from a broad profile with the largest gradients at the edge at low β to a triangular shaped profile with $\beta \sim \beta_{Troyon}$. Figure 2a shows the electron pressure profile at the time of maximum β as measured by the LIDAR diagnostic. The pressure gradient is almost constant across the minor radius but is larger in the plasma centre. The peaking factor β_0/β of this profile is 4.0. For the equilibrium reconstruction, this pressure profile is mapped onto a radial flux coordinate and averaged over the left and right side to obtain a symmetric pressure profile. This removes the local perturbations on the profile which are perhaps due to MHD activity. The q-profile resulting from an equilibrium fit to the magnetics and the pressure profile is shown in Fig. 2b. The positions of the $q = 1.0, 1.5$ and 2.0 surfaces agree well with the position of the perturbations on the pressure profile. To calculate the ballooning stability boundary, we start from the experimental pressure profile and change the pressure gradient locally

in small steps up to the ballooning limit. The resulting pressure profile is marginally stable over the whole minor radius. During the iteration the q-profile is kept essentially constant in the core but varies slightly in the outer regions to maintain the constraint of constant total current. In this way the shear of the final q-profile is slightly higher near the edge compared with the original q-profile (but the resulting β–limit ($\propto I/aB$) is not increased, as would be the case with a flux conserving iteration due to an increase in the total current).

In Fig. 3 the resulting marginally stable profile of the normalized pressure gradient (α) is compared with the experimental profile of the pressure gradient (here $\alpha = 4q^{*2}\sqrt{\psi}/(\epsilon B_0^2)dp/d\psi$ where $q^* = aLB_0/\mu_0 R_0 I_p$ and L is the length of the plasma circumference). This shows that the plasma is marginally stable to $n = \infty$ ballooning modes over more than 50% of the minor radius. In the plasma centre the experimental pressure gradient (determined from the normalised electron LIDAR pressure) exceeds the ballooning limit, even if the ballooning boundary is calculated with $q_0 = 1.05$ instead of the $q_0 = 0.95$ shown in Fig. 3. The β corresponding to the theoretically the marginally stable discharge is 6.3% which is $4.0I/(aB)$, comparable with the Sykes limit (Wesson and Sykes 1985). Discharges at, or slightly above, this Sykes limit have been observed in the D-III-D tokamak [Ferron et al 1990].

Even larger central pressure gradients have been produced in a high-β discharge where a pellet was injected just before 14 MW of additional neutral beam heating was applied. The electron pressure profile at maximum β (0.80 β_{Troyon}), is shown in Fig. 4. The peaking factor of this profile is 4.5. Calculation of the ballooning boundary in the plasma centre by lowering the local pressure gradient until stability is obtained shows that the maximum gradient exceeds the ballooning limit by almost a factor of 2. In this pellet case the theoretical condition for ballooning instability persists even when q on axis is varied to a value above one [which may be consistent with measurements and the observed $n = 1$ activity, (see next Section)]. Yet, experimentally no large degradation of confinement is observed until a large $n = 1$ mode causes a β-collapse (see next section). A possible explanation within the ideal MHD model is to assume that the q-profile is non-monotonic with negative global shear in the region of the large gradients [Roy et al 1988]. To study this possibility, instead of calculating a marginal pressure profile, we calculated the marginally stable q-profile. The resulting q-profile is shown in Fig. 5. It is the amplitude of the negative shear which dominantly determines the stability, the results being relatively insensitive to the absolute values of q_0 and q_{min} . The hollow current density profile needed for such a q-profile could be provided by the bootstrap current driven by the large gradients [Stubberfield et al., 1989].

In connection with the apparent experimental crossing of the theoretical ballooning boundary, it is to be noted that the stability boundaries obtained for both discharges pertain to modes in the limit $n \to \infty$. The growth rate of the finite-n ballooning mode decreases linearly with $1/n$. The critical mode number of the marginally stable mode,

below which the modes are stable, is given by [Connor et al., 1979]:

$$n_c = \frac{1}{2|\nu'|\omega_0^2}\left(\frac{\partial^2\omega^2}{\partial\psi^2}\frac{\partial^2\omega^2}{\partial\theta^2}\right)^{1/2}, \qquad (1)$$

where the quantities are evaluated at the flux surface with the largest growth rate, ν' is the local shear, and θ_0 is an integration constant related to the radial wave vector. For both discharges discussed above the critical mode number is of the order of 100–200, depending on the actual q–profile. Because of these large mode numbers, together with the fact that the instabilities occur in the centre, the finite-n unstable ballooning mode will have a width of the order of a few times the ion larmor radius. Therefore stabilisation of the ballooning mode by finite larmor radius effects can become important [Hastie et al., 1981]. Previous results showed that the large pressure gradients, produced by pellet injection into a discharge followed by strong additional heating (with a maximum $\beta \sim 0.4\beta_{Troyon}$), were limited by the ideal ballooning limit [Huysmans et al., 1989]. The difference between the previous pellet discharges at lower β and the present high-β discharges, is that the region of the large gradients of the previous discharges are localized more to the outside at a larger shear and with a higher q_0 (~ 1.2). In these cases the critical mode number is much lower ($n_c \sim 7$) and FLR effects are not likely to stabilise the mode.

A non-ideal effect which has not been taken into account is the effect of the fast particles. For the high-β discharges discussed in this paper, the fast particle pressure can be as large as 25% of the total pressure and is expected to be stabilising [Rosenbluth et al., 1983].

In a discharge at higher current, $I_P = 3$MA (and a higher startup density), the pressure profile remains broad with large pressure gradients near the edge, up to a disruption caused by the influx of carbon impurities. The pressure profile in this discharge is similar to the pressure profiles of the early phase of the high-β discharges discussed above. The maximum β obtained in this type of discharge is about 0.7 β_{Troyon}. The experimental and theoretical marginally stable profiles of the normalised pressure gradient (α) are shown in Fig. 6. The large gradients near the plasma edge are close to marginal stability in a small region with a width of approximately 15 cm. In this case the maximum β stable to ballooning modes ($\beta_{max} = 3.4I/aB_0$) is much higher than the experimentally achieved value; though it should be noted that the disruption apparently terminated the discharge before the β–limit was reached.

IV Low–n Stability

The low–n activity divides into that seen during β–saturation (fishbones, ELM's and sawteeth) and that seen during the β–collapse (large n =1, 2 or 3 activity) [Smeulders et al 1990]. For equilibria reconstructed to fit the β–saturation shots, with $q_0 < 1$, we find that the peaked pressure profiles cause the $n = 1$ internal kink to be strongly unstable.

This $n = 1$ instability is probably linked to the observed fishbone/sawtooth activity, but trapped particle effects must be included before a quantitative comparison can be made.

In the majority of cases in which β collapses there is large scale $n = 2$ activity present, however first we discuss a discharge in which a very large $n = 1$ mode ($\tilde{B}_\theta > 25$G) seems to limit the β. This case is the peaked pressure profile pellet case discussed in Section III (cf. Fig. 4). The pellet causes a reduction in l_i of ~ 0.2 and the polarimetry indicates an increase of ~ 0.2 in q_0. Subsequent to the pellet injection, as the β rises to $0.8\beta_{Troyon}$, a large $n = 1$ mode grows to $\tilde{B}_\theta \sim 25$G (by which time it is locked) and a collapse in β follows. This very large $n = 1$ mode is visible on the soft X-ray (SXR) array; a tomographic reconstruction shows a distortion to the core and island–like structures near $q = 2$ (Fig 7a). We have constructed an equilibrium for use in studying the stability of this case by matching the boundary shape, q_ψ and β_p, determined from the magnetics, and have also matched the LIDAR pressure profile and the location of $q = 2$ and 3 surfaces (from the SXR's). This leaves the form of the central–q to be determined. We have tried a flat central–q (with $q_0 \sim 1.0$), a parabolic central–q with ($q_0 \sim 0.9$) and a non-monotone q. From the $n = 1$ eigenfunctions for each class of q–profile, calculated with the linear FAR code, we have reconstructed the flux surface distortions. We find only the flat central–q, with $q_0 \sim 1.1$, gives a good match to the relative phase and amplitude between the core and $q = 2$ distortions in Fig 7(a); the theory result for $q_0 = 1.1$ (flat q) is shown in Fig 7(b). For the non-monotone q the relative phase of the core and $m = 2$ distortions is incorrect, while the monotone case shows no evident $m = 2$ islands. The flat central–q case shown in Fig 7(b) is close to the marginal threshold for the $n = 1$ mode; raising q_0 slightly leads to stability. The mode in this case is ideally unstable although the small resistivity (magentic Reynolds number $S = 10^6$) permits tearing at $q = 2$. The relatively high value of central–q ($q_0 = 1.1$) to obtain a match to the SXR tomography is consistent with the l_i and polarimetry measurements and also with the observed absence of sawteeth following the pellet injection.

For the $n = 2$ activity which generally seems to cause the β–collapse, we have also constructed equilibria by the technique described above for the $n = 1$ mode and considered a range of central q–profiles. The central q–profile was essentially treated as a free parameter which was determined by fitting to the SXR data. It should be noted that sawteeth can occur during large $n = 2$ activity which suggests that $q_0 < 1$. Figure 8 shows the $n = 1$ and $n = 2$ growth rates as a function of central–q, calculated with the FAR code (Charlton et al 1990), for a sequence in which the $q = 1$ radius is fixed at $r_1/a \sim 0.4$ for $q_0 \leq 0.97$. For $q_0 > 0.97$ the q–profile is varied by multiplying by a constant. From Fig 8 it can be seen that for $q_0 > 0.93$ the $n = 2$ growth rate ($\gamma_{n=2}$) exceeds the $n = 1$ growth rate ($\gamma_{n=1}$). The modes in this range ($\gamma_{n=2} > \gamma_{n=1}$) are ideally unstable and are the so-called infernal modes (Manickam et al 1987) which are driven by pressure gradient in low shear regions. These infernal modes are toroidally coupled but the $m = n$ mode is dominant. Figure 9 shows flux surfaces in the mid-plane versus toroidal angle for the $n = 2$ mode at $q_0 = 0.96$ (where $\gamma_{n=2} > \gamma_{n=1}$). In Fig 9 the dominant $m = 2$, $n = 2$

islands and the sideband $m = 3,4$ ($n = 2$) islands are clearly visible.

Experimentally during the large $n = 2$ magnetic activity which precedes a β–collapse large $n = 2$ oscillations are also observed in the SXR data. Results from the vertical SXR camera during such $n = 2$ activity are shown in Fig 10(a). To compare these results with theoretical predictions we have reconstructed the line integrated SXR's by assuming the emissivity on a given field line is a constant, which is a function of the average radius of that field line. This functional form is chosen to give an approximate match to the observed line integrated emissivities (although the slight central hollow in the experimental measurement is not reproduced). The line integrated SXR chords corresponding to the case shown in Fig 9 are given in Fig 10(b). It can be seen that the theoretically constructed SXR chords (Fig 10(b)) reproduce many of the features of the experimental (Fig 10(a)) SXR chords. To make this comparison more quantitative the relative phase of the signals shown in Fig 10 are compared in Fig 11; the core region is omitted because the experimental phases become indeterminate and also because, as mentioned above, the theoretical emissivity does not reproduce the slight hollow observed experimentally. The reasonable agreement in Fig 11 suggests that the low shear infernal modes are a likely candidate for the observed $n = 2$ activity. We have examined the sensitivity of the SXR fit by examining other q–profiles. For example we have checked the case shown in Fig 9 when $q_0 = 0.91$. In this case the modes are resistive ballooning modes with $\gamma_{n=2} < \gamma_{n=1}$ (which of course contradicts the experimental dominance of the $n = 2$ mode) and the reconstructed SXR's show phase inversions which do not agree with the experiment. The small increases in central-q to trigger the $n = 2$ instability to be dominant ($\Delta q \sim 0.02$) may be produced by the large sawtooth which often initiates the n=2 activity [Smeulders et al 1990].

V Summary

The ballooning stability studies typically show that at the highest values of β obtained in JET so far, the pressure profiles are marginally stable to ballooning modes over the central 50% of the plasma when $\beta \sim \beta_{Troyon}$. In a number of discharges the large pressure gradients in the core region exceed the ideal $n = \infty$ ballooning stability limit by a considerable amount. However, this only happens when n_c is large so that stabilization of the high-n mode numbers by finite larmor radius effects or fast particles should be important. For a pellet shot, in which an $n = 1$ mode is strongly unstable, stability calculations show that the SXR tomographic results are reproduced best by a flat central–q with $q_0 \sim 1.1$. For $n = 2$ modes which usually cause the β–collapse and seem often to be initiated by a sawtooth [1], flat q–profiles (with $q_0 \sim 0.96$) seem to give the best agreement with SXR's.

In these studies we have not addressed the effects of the hot trapped particle population on the stability. Studies of these effects on the ballooning mode and $n = 1$ internal kink are in progress, and will be reported elsewhere.

Acknowledgement

We are grateful to the JET diagnostic and operating teams for the use of their data, and in particular to the LIDAR group for the pressure profile data. We should also like to thank the Lausanne group for providing us with a copy of the ERATO code. The Culham authors were supported under a task agreement with the JET Joint Undertaking.

References

Blum J, Gilbert J C, Le Foll J and Thooris B (1986) 8^{th} Europhys Conf on Comp Phys Computing in Plasma Physics, Eibsee, Vol 10D, 49.

Charlton L A, Holmes J A, Lynch V E, Carreras B A and Hender T C, (1990) Jrnl Comp Phys **86**, 270.

Connor J.W., Hastie R.J. and Taylor J.B., (1979) Proc. Roy. Soc Lond. **A. 365**, 1-17.

Ferron J.R, Chu M.S., Helton F.J. Howl W., Kellman A.G., Lao L.L., Lazarus E.A., Lee J.K. Osborne T.H., Stambaugh R.D., Straight E.J., Taylor T.S., and Turnbull A.D., (1990) Proc. 17th EPS Conf. on Contr. Fusion and Plasma Heating, p. 371.

Goedbloed J.P. (1981), Comp. Phys. Commun. **24**, 311.

Goedbloed J.P., Hogewey G.M.D., Kleibergen R., Rem J., Galvao R.M.O., Sakanaka P.H. (1984), Proc. 10th International IAEA Conf. on Plasma Physics and Contr. Nucl. Fusion Research, London, Vol. II, p. 165, IAEA , Vienna, 1985.

Gruber R, Troyon F, Berger D, Bernard L C, Rousett S, Schreiber R, Kerner W, Schneider W, and Roberts K V (1981) Comp Phys Comm **21** 323.

Hastie R.J. and Hesketh K.W., (1981) Nucl. Fusion 21, **6** 651.

Huysmans G.T.A., Galvao R.M.O., Goedbloed J.P., Lazzaro E. and Smeulders P., (1989) Plasma Physics and Contr. Fusion, **31** 2101.

Huysmans G.T.A., Galvao R.M.O., and Goedbloed J.P., (1990) 'High β stability studies of JET discharges' Rijnhuizen Report, 90–193.

Lazzaro E., and Mantica P., (1988) Plasma Phys and Contr Fus **30** 1735.

Manickam J., Pomphrey N., and Todd A.M.M., 1987 Nuclear Fus **27** 1461-1472.

Rosenbluth M.N., Tsai S.T., Van Dam J.W., and Engquist M.G., Phys. Rev. Lett. (1983) 51 1967.

Roy A. and Troyon F., Proc. Joint Varenna-Lausanne Workshop on Theory of Fusion Plasmas, October 1988.

Smeulders P., Adams J.M., Balet B., Campbell D., Cheetham A., Corti S., Edwards A., Gottardi N., Gowers C., Hender T.C., Huysmans G., Jacquinot J., Joffrin E., Kwon O.,Lazzaro E., Marcus F.B., Morgan P., Nave F., Nielson P., O'Brien D., O'Rourke J., Porcelli F., Porte L., Sadler G., Sips G., Start D., Tanga A., Ward D., and Weisen H., (1990) Proceedings of 17th EPS Conference on Controlled Fusion and Plasma Heating Part I, p.323.

Stubberfield P.M., Balet B., Campbell D., Challis C.D., Cordey J.G., Hammett G., O'Rourke J., and Schmidt G.L., (1989) Proc. 16th EPS Conf. on Contr. Fusion and Plasma Physics, 253.

Troyon F., Gruber R., Saürenamnn H., Semenzato S., and Succi S., (1984) Plasma Phys and Contr Fusion **26**, 209. Wesson J A and Sykes A, 1985 Nucl Fusion **25** 85-88.

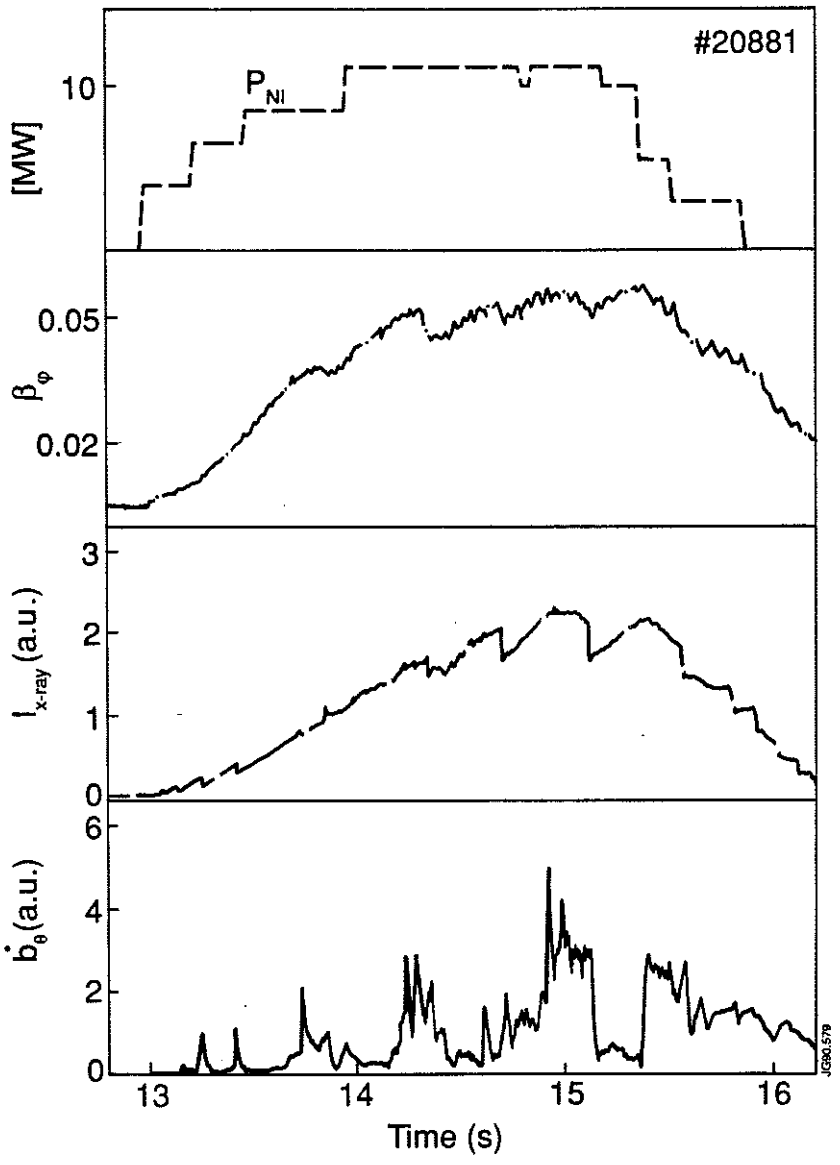

Fig. 1 Time traces of the toroidal β, the total heating power and the general MHD activity of discharge #20881, I_p =2MA, $B_T = 1.3 \rightarrow 1.0$T (ramped down).

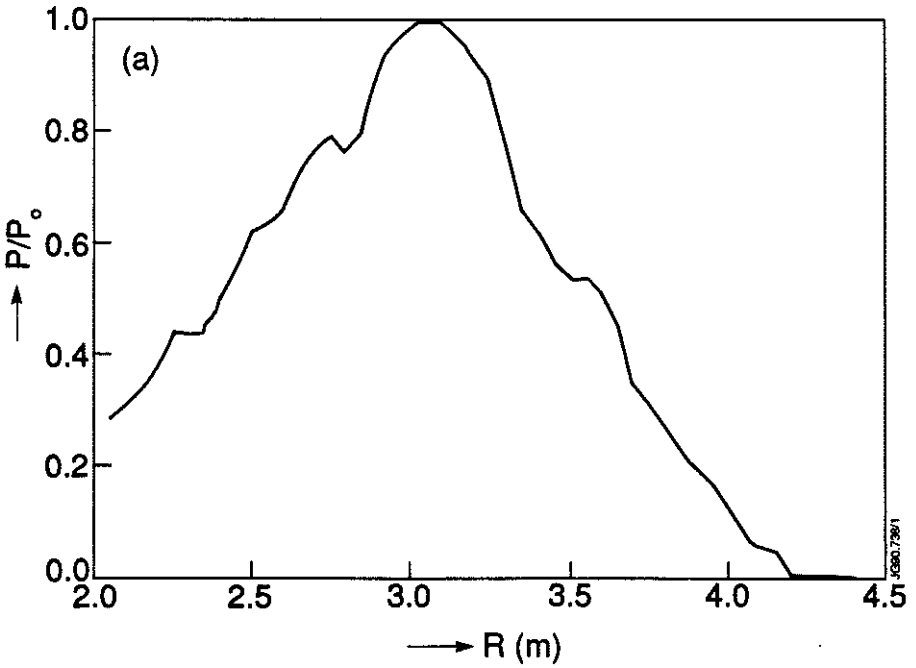

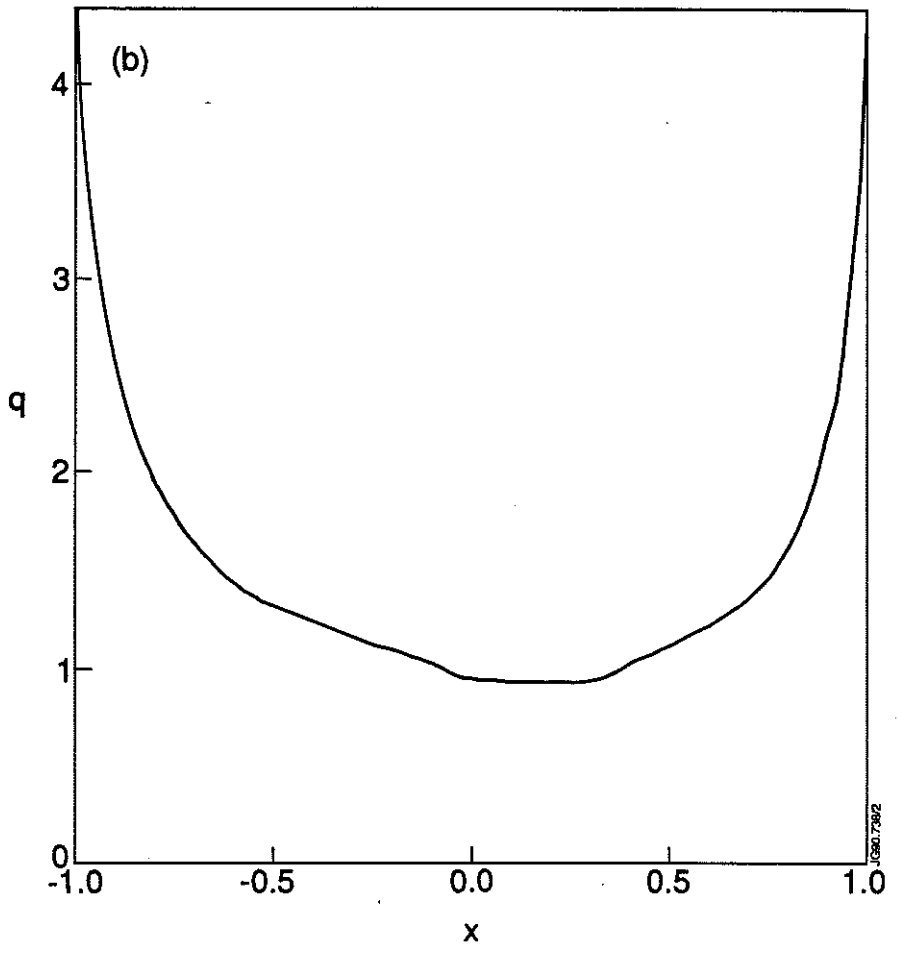

Fig. 2 (a) The electron pressure profile of discharge #20272, at the time (t=52.5s) of maximum β. (b) The reconstructed q-profile of discharge #20272, at maximum β. Here X is the normalised minor radius.

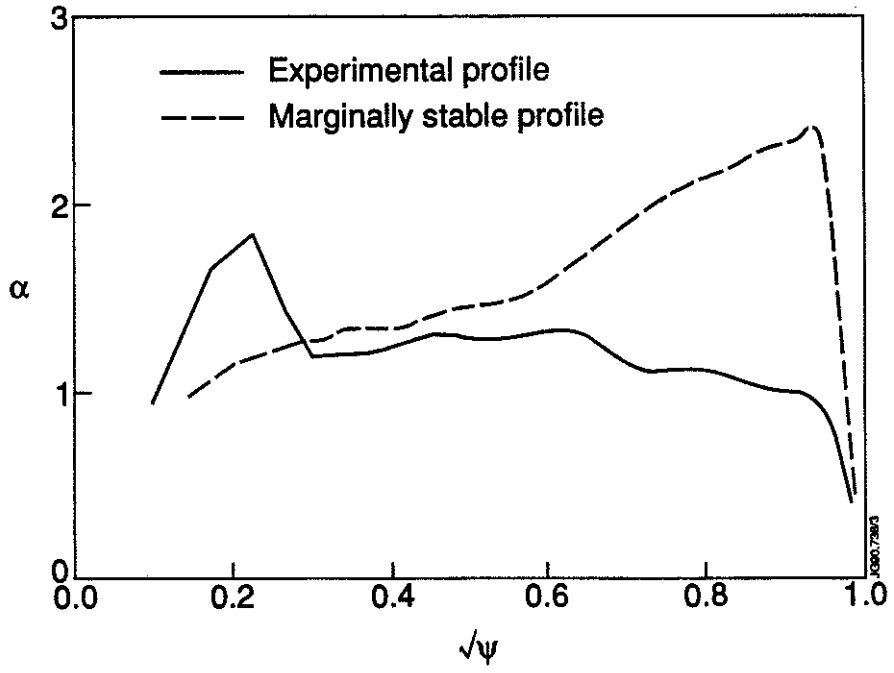

Fig. 3 The profiles of the experimental and the marginally stable normalized pressure gradient (α) as a function of $\sqrt{\psi}$ of discharge #20272 with a triangular pressure profile.

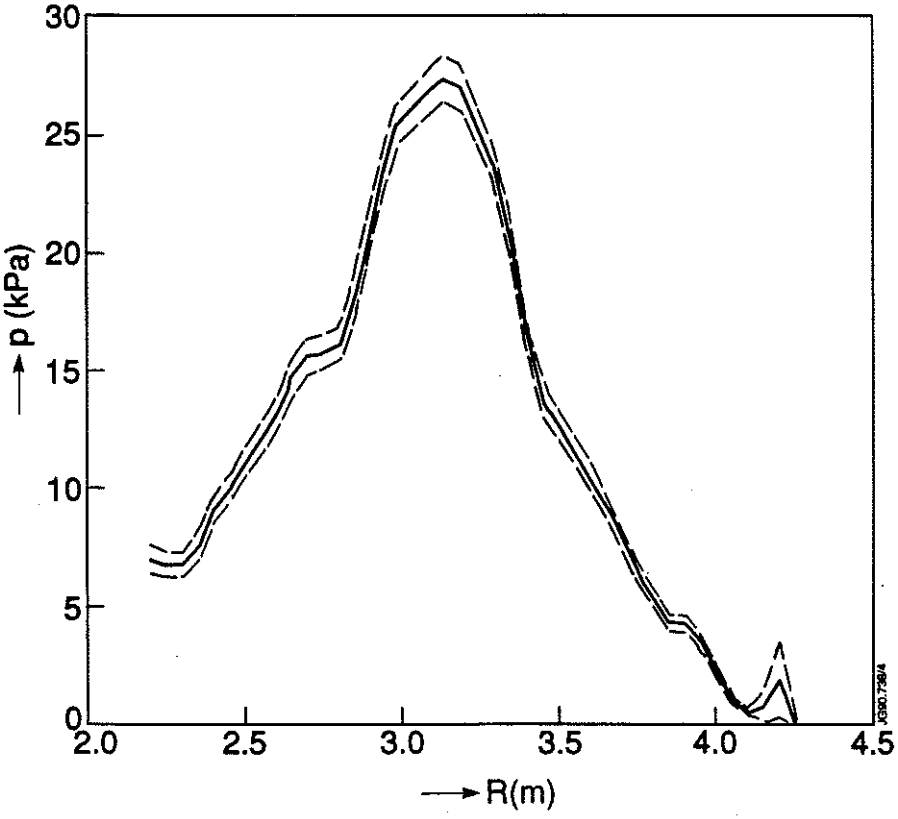

Fig. 4 The peaked pressure profile of the high-β discharge #20302 with pellet injection (full line). Included are the upper and lower error boundaries.

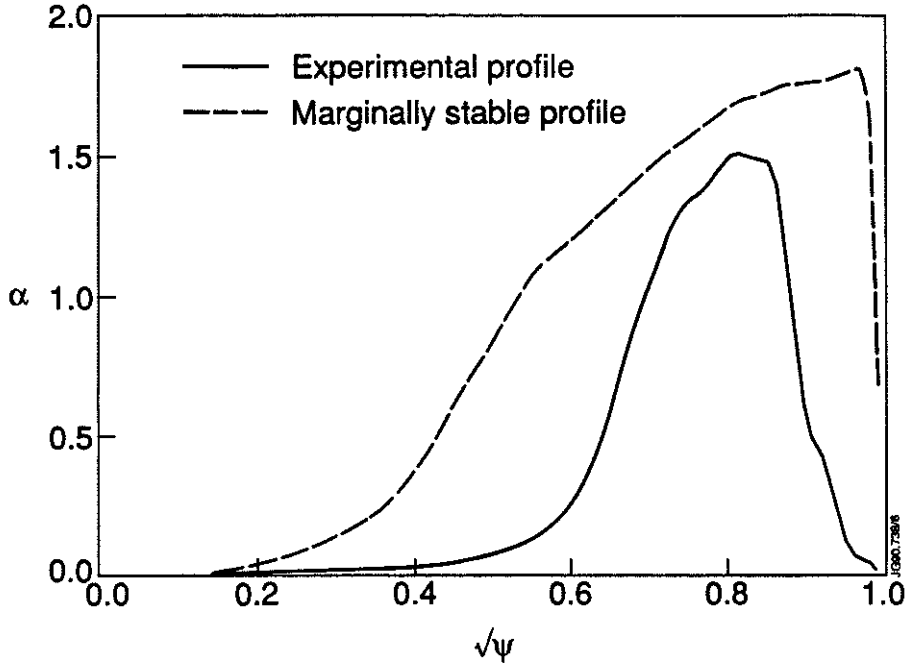

Fig. 5 The q-profile for which the pressure profile of Fig. 4 is marginally stable to ballooning modes in the plasma centre.

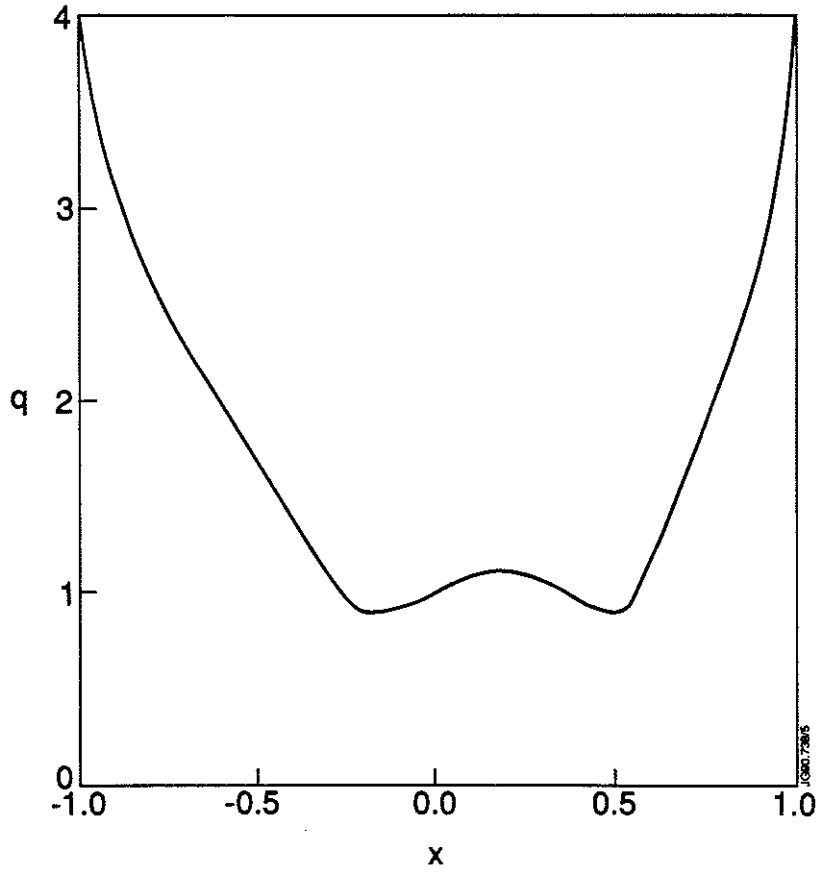

Fig. 6 The profiles of the experimental and marginally stable normalized pressure gradient versus $\sqrt{\psi}$ of discharge #19970 with a broad pressure profile.

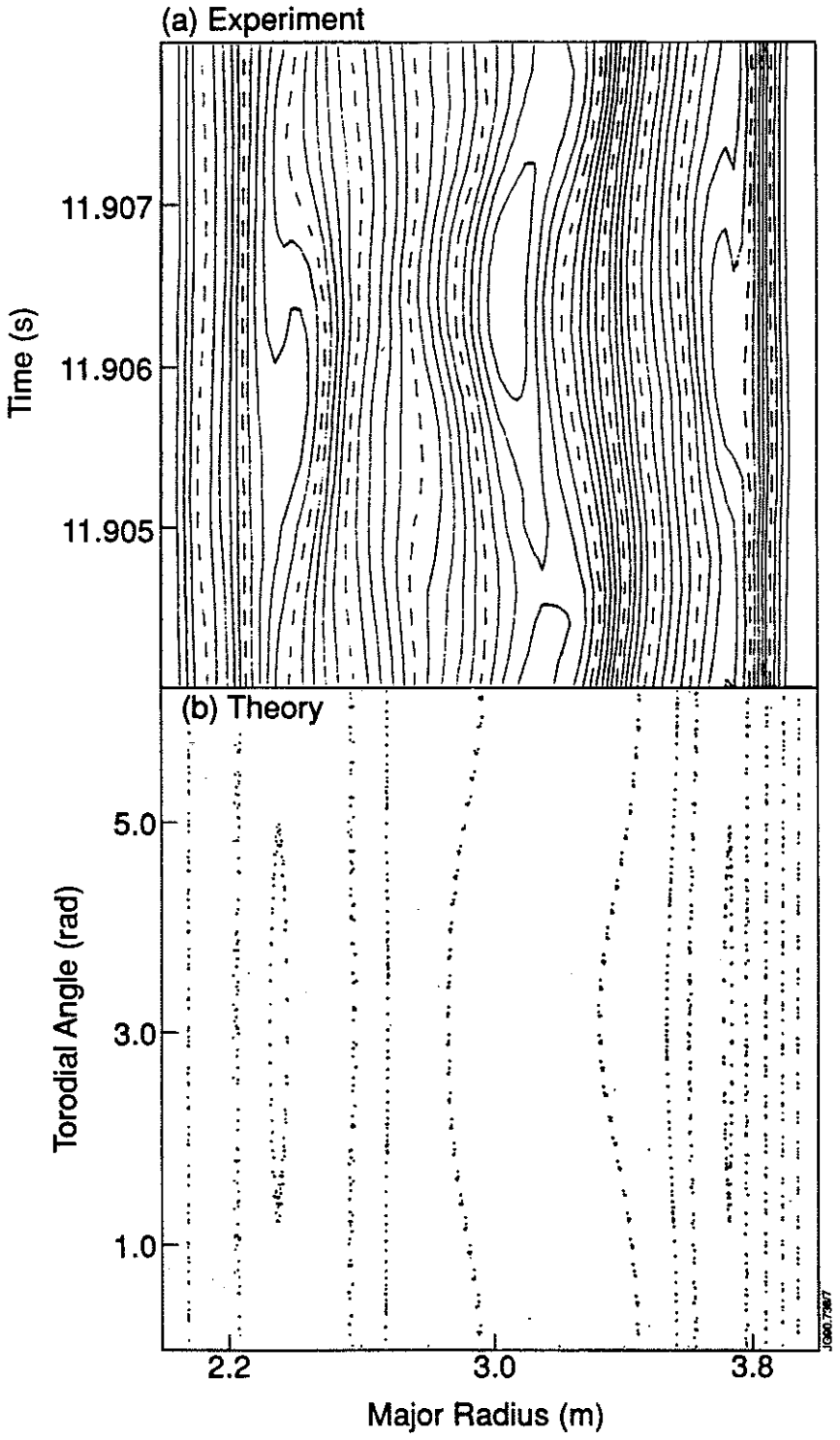

Fig. 7 (a) Tomographic reconstruction of SXR emissivity in the horizontal mid–plane during large $n = 1$ activity (Shot 20302) [the island structure at $R \sim 3.1$m is caused by the SXR emissivity increasing and decreasing as the axis moves in and out]. (b) Flux surfaces resulting from $n = 1$ mode for low shear q–profile in horizontal mid–plane. N.B. The dominant toroidal rotation gives an equivalence between time of viewing and toroidal angle of view.

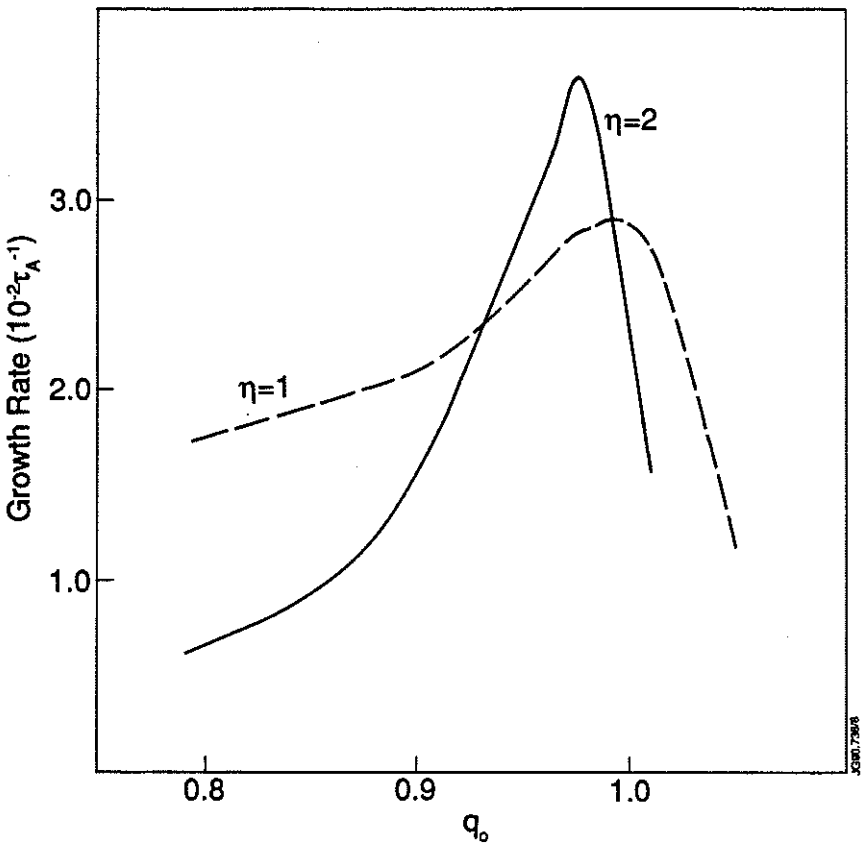

Fig. 8 Growth rate of $n = 1$ ($\gamma_{n=1}$) and $n = 2$ ($\gamma_{n=2}$) modes as the central–q is varied For low shear ($q_0 > 0.93$) the $n = 2$ mode is dominant.

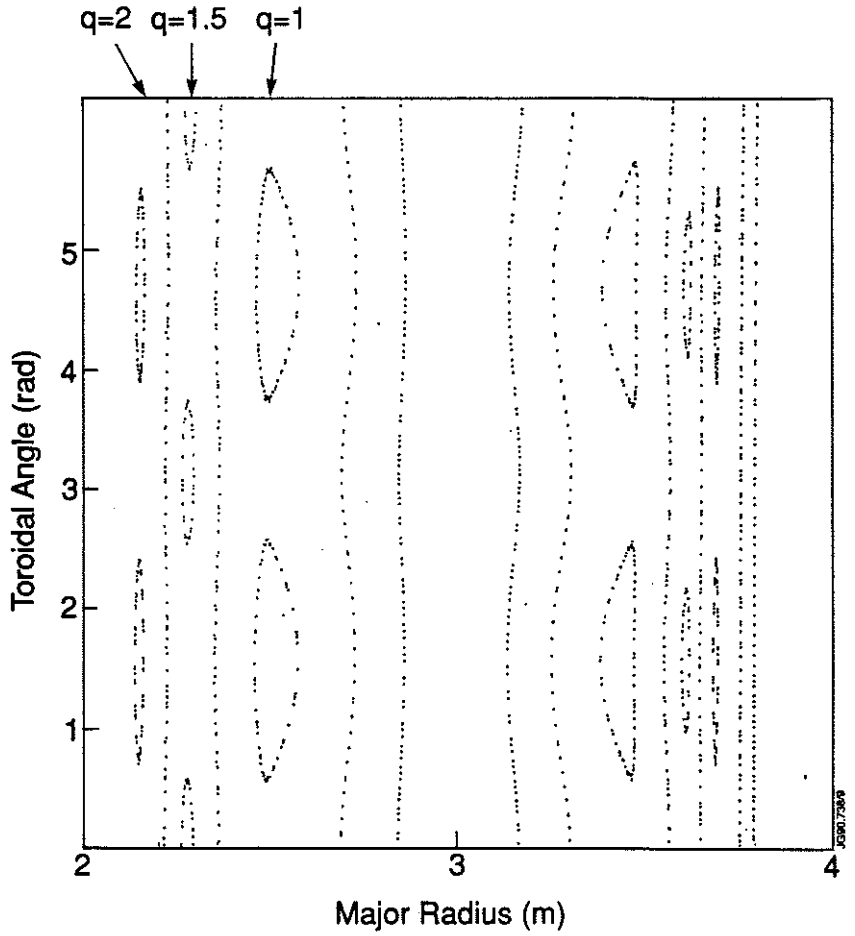

Fig. 9 Flux surfaces for $n = 2$ mode in the horizontal mid–plane.

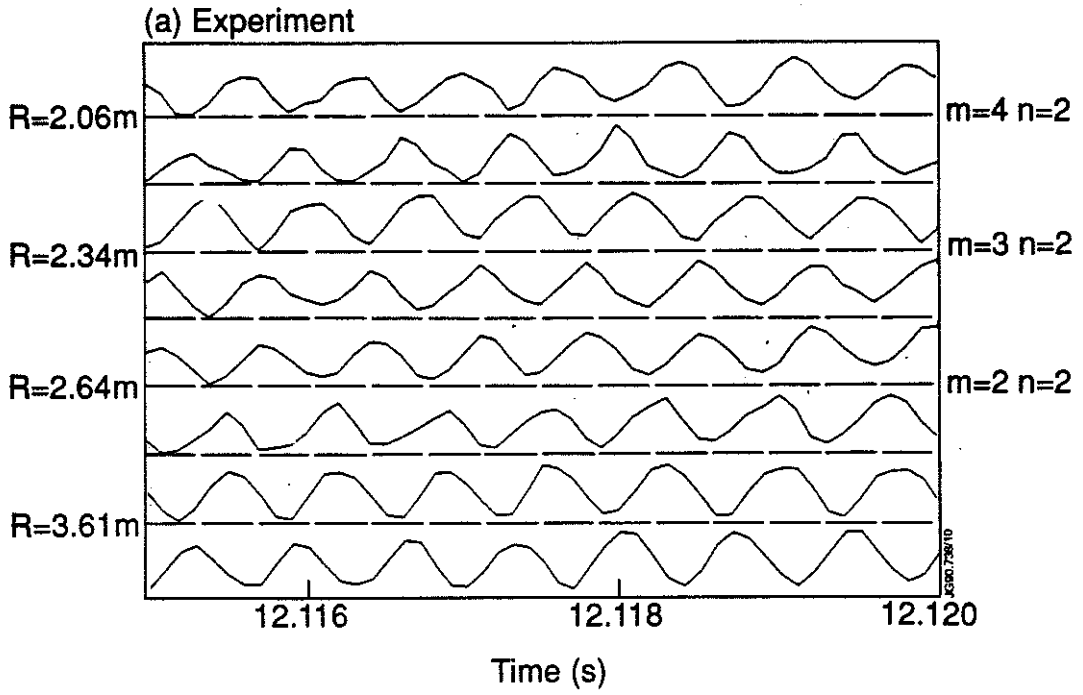

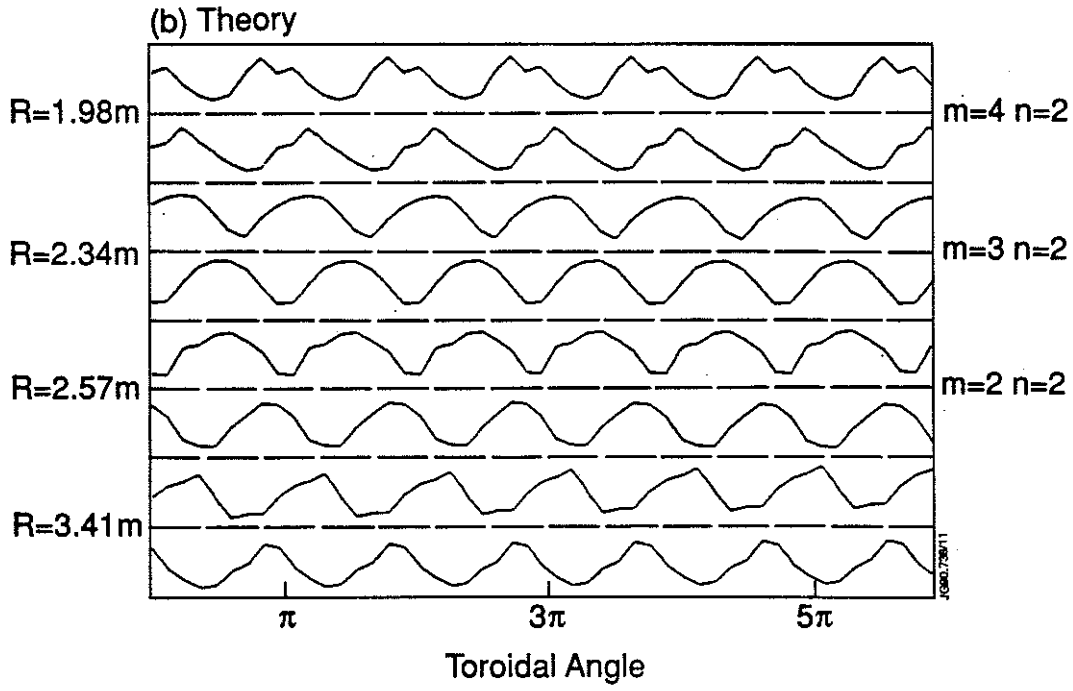

Fig. 10 (a) Vertical SXR chords during $n = 2$ activity; note the multiple phase inversions. (b) Theoretically reconstructed SXR chords corresponding to the flux surfaces shown in Fig. 9. The radii (R) are obtained from where the chords intercept the horizontal mid-plane.

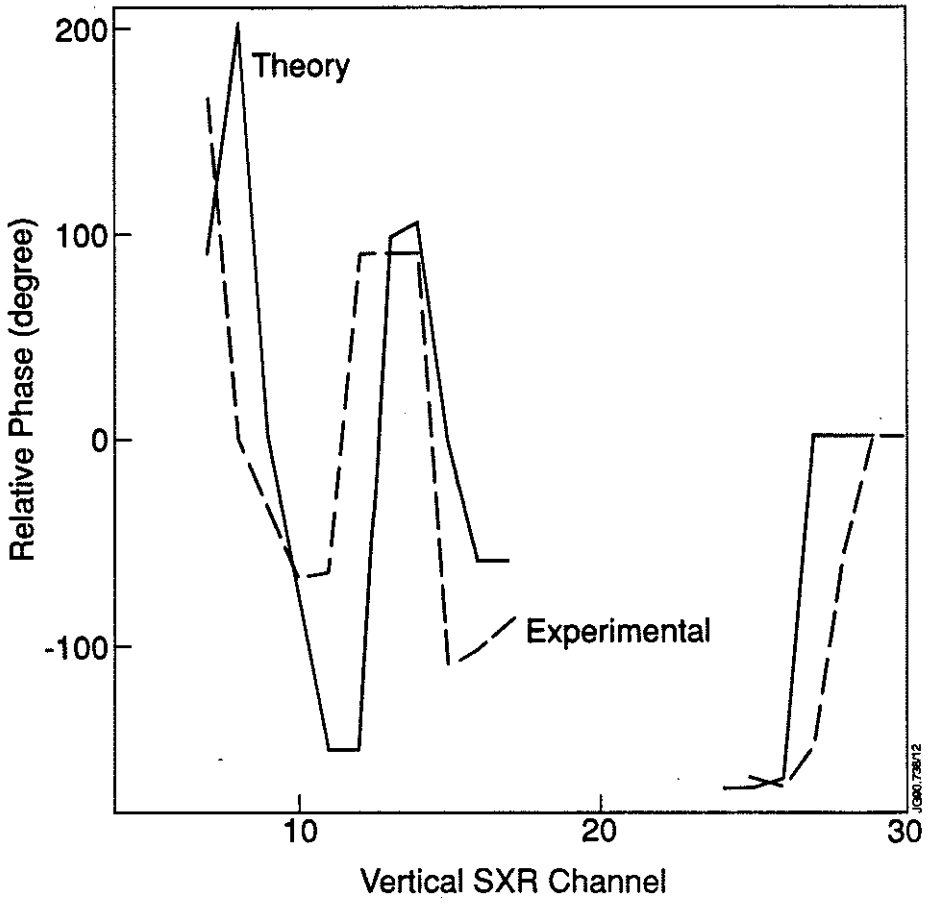

Fig. 11 Relative phase of SXR chords from experiment (Fig. 10(a)) and theory (Fig. 10(b)).

APPENDIX 1.

THE JET TEAM

JET Joint Undertaking, Abingdon, Oxon, OX14 3EA, U.K.

J.M.Adams[1], F.Alladio[4], H.Altmann, R.J.Anderson, G.Appruzzese, W.Bailey, B.Balet, D.V.Bartlett, L.R.Baylor[24], K.Behringer, A.C.Bell, P.Bertoldi, E.Bertolini, V.Bhatnagar, R.J.Bickerton, A.Boileau[3], T.Bonicelli, S.J.Booth, G.Bosia, M.Botman, D.Boyd[31], H.Brelen, H.Brinkschulte, M.Brusati, T.Budd, M.Bures, T.Businaro[4], H.Buttgereit, D.Cacaut, C.Caldwell-Nichols, D.J.Campbell, P.Card, J.Carwardine, G.Celentano, P.Chabert[27], C.D.Challis, A.Cheetham, J.Christiansen, C.Christodoulopoulos, P.Chuilon, R.Claesen, S.Clement[30], J.P.Coad, P.Colestock[6], S.Conroy[13], M.Cooke, S.Cooper, J.G.Cordey, W.Core, S.Corti, A.E.Costley, G.Cottrell, M.Cox[7], P.Cripwell[13], F.Crisanti[4], D.Cross, H.de Blank[16], J.de Haas[16], L.de Kock, E.Deksnis, G.B.Denne, G.Deschamps, G.Devillars, K.J.Dietz, J.Dobbing, S.E.Dorling, P.G.Doyle, D.F.Düchs, H.Duquenoy, A.Edwards, J.Ehrenberg[14], T.Elevant[12], W.Engelhardt, S.K.Erents[7], L.G.Eriksonn[5], M.Evrard[2], H.Falter, D.Flory, M.Forrest[7], C.Froger, K.Fullard, M.Gadeberg[11], A.Galetsas, R.Galvao[8], A.Gibson, R.D.Gill, A.Gondhalekar, C.Gordon, G.Gorini, C.Gormezano, N.A.Gottardi, C.Gowers, B.J.Green, F.S.Griph, M.Gryzinski[26], R.Haange, G.Hammett[6], W.Han[9], C.J.Hancock, P.J.Harbour, N.C.Hawkes[7], P.Haynes[7], T.Hellsten, J.L.Hemmerich, R.Hemsworth, R.F.Herzog, K.Hirsch[14], J.Hoekzema, W.A.Houlberg[24], J.How, M.Huart, A.Hubbard, T.P.Hughes[32], M.Hugon, M.Huguet, J.Jacquinot, O.N.Jarvis, T.C.Jernigan[24], E.Joffrin, E.M.Jones, L.P.D.F.Jones, T.T.C.Jones, J.Källne, A.Kaye, B.E.Keen, M.Keilhacker, G.J.Kelly, A.Khare[15], S.Knowlton, A.Konstantellos, M.Kovanen[21], P.Kupschus, P.Lallia, J.R.Last, L.Lauro-Taroni, M.Laux[33], K.Lawson[7], E.Lazzaro, M.Lennholm, X.Litaudon, P.Lomas, M.Lorentz-Gottardi[2], C.Lowry, G.Magyar, D.Maisonnier, M.Malacarne, V.Marchese, P.Massmann, L.McCarthy[28], G.McCracken[7], P.Mendonca, P.Meriguet, P.Micozzi[4], S.F.Mills, P.Millward, S.L.Milora[24], A.Moissonnier, P.L.Mondino, D.Moreau[17], P.Morgan, H.Morsi[14], G.Murphy, M.F.Nave, M.Newman, L.Nickesson, P.Nielsen, P.Noll, W.Obert, D.O'Brien, J.O'Rourke, M.G.Pacco-Düchs, M.Pain, S.Papastergiou, D.Pasini[20], M.Paume[27], N.Peacock[7], D.Pearson[13], F.Pegoraro, M.Pick, S.Pitcher[7], J.Plancoulaine, J-P.Poffé, F.Porcelli, R.Prentice, T.Raimondi, J.Ramette[17], J.M.Rax[27], C.Raymond, P-H.Rebut, J.Removille, F.Rimini, D.Robinson[7], A.Rolfe, R.T.Ross, L.Rossi, G.Rupprecht[14], R.Rushton, P.Rutter, H.C.Sack, G.Sadler, N.Salmon[13], H.Salzmann[14], A.Santagiustina, D.Schissel[25], P.H.Schild, M.Schmid, G.Schmidt[6], R.L.Shaw, A.Sibley, R.Simonini, J.Sips[16], P.Smeulders, J.Snipes, S.Sommers, L.Sonnerup, K.Sonnenberg, M.Stamp, P.Stangeby[19], D.Start, C.A.Steed, D.Stork, P.E.Stott, T.E.Stringer, D.Stubberfield, T.Sugie[18], D.Summers, H.Summers[20], J.Taboda-Duarte[22], J.Tagle[30], H.Tamnen, A.Tanga, A.Taroni, C.Tebaldi[23], A.Tesini, P.R.Thomas, E.Thompson, K.Thomsen[11], P.Trevalion, M.Tschudin, B.Tubbing, K.Uchino[29], E.Usselmann, H.van der Beken, M.von Hellermann, T.Wade, C.Walker, B.A.Wallander, M.Walravens, K.Walter, D.Ward, M.L.Watkins, J.Wesson, D.H.Wheeler, J.Wilks, U.Willen[12], D.Wilson, T.Winkel, C.Woodward, M.Wykes, I.D.Young, L.Zannelli, M.Zarnstorff[6], D.Zasche[14], J.W.Zwart.

PERMANENT ADDRESS

1. UKAEA, Harwell, Oxon. UK.
2. EUR-EB Association, LPP-ERM/KMS, B-1040 Brussels, Belgium.
3. Institute National des Récherches Scientifique, Quebec, Canada.
4. ENEA-CENTRO Di Frascati, I-00044 Frascati, Roma, Italy.
5. Chalmers University of Technology, Göteborg, Sweden.
6. Princeton Plasma Physics Laboratory, New Jersey, USA.
7. UKAEA Culham Laboratory, Abingdon, Oxon. UK.
8. Plasma Physics Laboratory, Space Research Institute, Sao José dos Campos, Brazil.
9. Institute of Mathematics, University of Oxford, UK.
10. CRPP/EPFL, 21 Avenue des Bains, CH-1007 Lausanne, Switzerland.
11. Risø National Laboratory, DK-4000 Roskilde, Denmark.
12. Swedish Energy Research Commission, S-10072 Stockholm, Sweden.
13. Imperial College of Science and Technology, University of London, UK.
14. Max Planck Institut für Plasmaphysik, D-8046 Garching bei München, FRG.
15. Institute for Plasma Research, Gandhinagar Bhat Gujat, India.
16. FOM Instituut voor Plasmafysica, 3430 Be Nieuwegein, The Netherlands.
17. Commissiariat à L'Energie Atomique, F-92260 Fontenay-aux-Roses, France.
18. JAERI, Tokai Research Establishment, Tokai-Mura, Naka-Gun, Japan.
19. Institute for Aerospace Studies, University of Toronto, Downsview, Ontario, Canada.
20. University of Strathclyde, Glasgow, G4 ONG, U.K.
21. Nuclear Engineering Laboratory, Lapeenranta University, Finland.
22. JNICT, Lisboa, Portugal.
23. Department of Mathematics, Univeristy of Bologna, Italy.
24. Oak Ridge National Laboratory, Oak Ridge, Tenn., USA.
25. G.A. Technologies, San Diego, California, USA.
26. Institute for Nuclear Studies, Swierk, Poland.
27. Commissiariat à l'Energie Atomique, Cadarache, France.
28. School of Physical Sciences, Flinders University of South Australia, South Australia SO42.
29. Kyushi University, Kasagu Fukuoka, Japan.
30. Centro de Investigaciones Energeticas Medioambientales y Techalogicas, Spain.
31. University of Maryland, College Park, Maryland, USA.
32. University of Essex, Colchester, UK.
33. Akademie de Wissenschaften, Berlin, DDR.

CR 88.49.1A